PAPER

Architecting hydrangea-inspired nitrogen-doped hollow carbon with isolated Co atoms for superior oxygen reduction catalysis†

Xiaolan Gao,‡[a] Yue Li,‡[b] Zhiqing Zhang,[a] Hao Zhang[b] and Ge Li*[a]

The oxygen reduction reaction (ORR) underpins energy technologies like metal–air batteries and fuel cells, yet it faces issues with slow kinetics and relies on costly, scarce noble metal catalysts. This work develops a facile approach by anchoring isolated Co atoms on defective nitrogen-doped carbon using low-temperature NH_4Cl pyrolysis along with metal ion adsorption. The as-prepared catalyst exhibits excellent ORR performance, achieving a high half-wave potential of 0.91 V in alkaline electrolytes and remarkable durability for 253 h with a retention of 97.47% at half-wave potential. Density functional theory (DFT) simulations confirm that the $Co–N_4$ moieties act as the active sites and elucidate substantial electronic structure modulations of Co centers during the ORR. These electronic structure modulations manifest as shifts in the Co atoms projected density of states and fluctuations in their local magnetic moments across various stages of the catalytic process. The findings presented herein advance both the practical synthesis of robust single-atom electrocatalysts and the theoretical understanding of their electronic structural properties.

1. Introduction

Promising energy conversion devices, such as fuel cells and metal–air batteries, provide environmentally benign alternatives with a minimal carbon footprint.[1–4] For years, researchers have been developing transition metal-based catalysts as substitutes for noble metal-based catalysts.[5–8] Various strategies have been employed, including material composite and heteroatom doping.[9–11] For example, transition metals (TMs) deposited on functionalized carbon (*e.g.*, nitrogen doping) substrates, such as carbon-supported TMs-N coordination catalysts, N-doped carbon nanotube-supported TM oxides, and polyaniline-based catalysts doped TMs, have shown high catalytic activity.[12–15]

Despite notable progress in improving transition metal ORR catalyst activity, low-atom-utilization efficiency and agglomeration issues remain common in prepared materials.[16–18] Catalytic activity predominantly occurs in surface-exposed atoms, while the interior atoms remain inaccessible to electrolyte interactions.[19–21] To address these limitations, single-atom catalysts (SACs) have emerged as an advanced platform, offering unprecedented atomic economy in catalytic processes. SACs have emerged as a frontier in heterogeneous catalysis, garnering significant research interest due to their exceptional catalytic properties.[22] These nanomaterials exhibit remarkable activity and selectivity across various reactions, stemming from their unique characteristics, including maximized atom utilization, uniform active sites, and distinctive electronic structures.[23–25] The potential of SACs in electrocatalysis, particularly for the oxygen reduction reaction (ORR), has been demonstrated through several groundbreaking studies. For example, Chen *et al.* developed homogeneous iridium porphyrin-like Ir–N–C SAC, achieving a notable mass activity of 12.2 A mg^{-1} Ir at 0.85 V for ORR.[26] Advancing the field further, Shao and colleagues employed a novel "ceria-assisted" strategy to synthesize Fe–N–C SACs with atomically dispersed Fe active sites, resulting in a catalyst with an impressive half-wave potential of 0.915 V for ORR.[27]

Despite their promising activity and potential as ORR catalysts, SACs still face critical issues that must be addressed: (1) the diverse coordination environments and defect types of various metal atoms make achieving a uniform distribution of single atoms challenging. (2) The activity and durability of SACs remain insufficient for commercial operations.[28–31] While plenty of studies have focused on SAC preparation, physical methods such as atomic layer deposition and chemical vapor deposition have drawbacks, including low production yields, complex production processes, and high cost.[32–35] Established synthetic protocols, notably the photochemical deposition technique, involve multi-step procedures that sequentially address precursor attachment, metal ion reduction, and engineering defect-enriched support structures. In contrast, the impregnation method, combined with

[a]Department of Mechanical Engineering, University of Alberta, Edmonton, Alberta, Canada. E-mail: ge.li@ualberta.ca

[b]Department of Chemical and Materials Engineering, University of Alberta, Edmonton, Alberta, Canada

‡ These authors equally worked in this work.

This journal is © The Royal Society of Chemistry 2025

J. Mater. Chem. A, 2025, **13**, 14631–14645 | **14631**

physical and chemical methods, requires less equipment and energy because of simpler processes and lower energy requirements.[35–38] The heavy reliance on rigorous environmental parameters, such as temperature and pH, makes this approach technically challenging.[39–43]

To advance the fundamental research and engineering applications of SACs, we developed hydrangea-inspired nitrogen-doped hollow carbon decorated with Co single atoms using an NH_4Cl-assisted pyrolysis and adsorption process. This rational design strategy achieves dual-parameter optimization by introducing NH_4Cl and controlling the incorporation of different amounts of Co elements, simultaneously modulating both the spatial density and surface accessibility of catalytically active sites.[44] The systematic variation of Co content serves as an

effective means to fine-tune these critical structural parameters.[45–48] As anticipated, the Co-SAC/NC exhibited a high half-wave potential of 0.91 V and demonstrated stable operation for up to 253 hours at this potential. Based on various physical and chemical characterizations, as well as computational simulations, the excellent ORR activity of the Co-SAC/NC catalyst can be attributed to the synergistic effect of its hollow porous structure and the high density of Co–N_4 sites confirmed by X-ray absorption fine structure (XAFS), density functional theory (DFT), and Brunauer–Emmett–Teller (BET) measurements. This optimized approach not only increases the density of active sites but also improves their accessibility, potentially leading to enhanced catalytic performance.
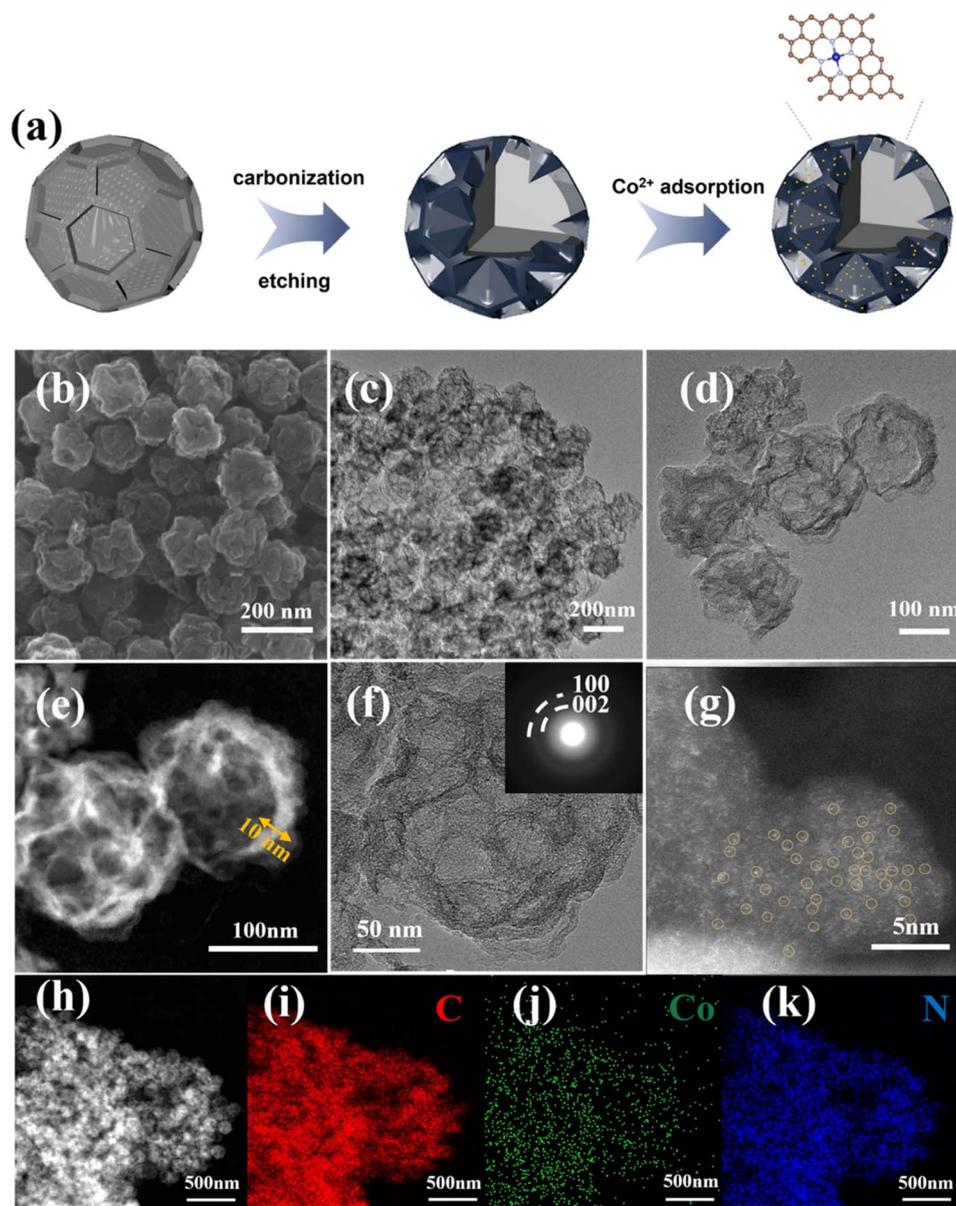

Fig. 1 Synthesis and morphology characterization of Co-SAC/NC. (a) Schematic illustration of the synthetic route. (b) SEM image. (c) and (d) TEM images, (e) HAADF-STEM image, (f) HR-TEM image, and SAED pattern (inset in (f)). (g) Aberration-corrected HAADF-STEM images (h)–(k) EDS elemental mappings.

14632 | J. Mater. Chem. A, 2025, 13, 14631–14645

This journal is © The Royal Society of Chemistry 2025

2. Results and discussion

2.1 Synthesis and characterization

Fig. 1a illustrates the synthesis route of hydrangea-like nitrogen-doped hollow carbon with Co single atoms (Co-SAC/NC) *via* a three-step process. First, a self-assembled precursor (NAP) was synthesized by coordinating organic linkers in methanol. The subsequent pyrolysis of the NAP template yielded a nitrogen-doped porous carbon framework rich in defect sites. Finally, atomic Co species were anchored within the nitrogen-rich framework through NH₄Cl-assisted low-temperature pyrolysis, forming well-dispersed Co–N₄ active sites. Notably, the NH₄Cl assistance enhanced the specific surface area of the catalyst, leading to increased exposure of the Co–N₄ active centers.[49] To understand the underlying mechanisms of the as-prepared Co, three other materials were used as comparison samples: (1) 1.91 wt.% of Co addition with less Co content to Co-SAC/NC is denoted as Co-LC/NC, (2) 5.41 wt.% of Co addition with more Co content to Co-SAC/NC is denoted as Co-cluster/NC, and (3) nitrogen-doped porous carbon framework is denoted as NC (Table S1 and Fig. S1–S3†). Fig. 1b–d presents the microstructural features of Co-SAC/NC, as revealed by scanning electron microscopy (SEM) and transmission electron microscopy (TEM) analyses. The Co-SAC/NC exhibits a unique hydrangea-like architecture with multilayered corrugated shells of about 10 nm thick and internal void spaces, as shown in Fig. 1e. The high-resolution transmission electron microscopy (HRTEM) images demonstrate abundant randomly distributed micropores (~1.8 nm) and lattice distortion defects (Fig. 1f). HRTEM analysis and selected area electron diffraction (SAED, inset in Fig. 1f) confirmed the absence of metallic Co or Co compound particles throughout the structure. Aberration-corrected high-angle annular dark-field scanning transmission electron microscopy (AC HAADF-STEM) imaging at sub-angstrom resolution revealed numerous bright spots, indicative of Co atoms (4.12 wt.%, Table S1†) dispersed on the NC support (Fig. 1g). Energy-dispersive X-ray spectroscopy (EDS) mapping confirmed the uniform distribution of Co, C, and N elements throughout the Co-SAC/NC structure (Fig. 1h).

Morphological analyses revealed that Co-cluster/NC, NC, and Co-LC/NC samples maintained consistent hierarchical architectures. This demonstrates that the structural integrity of the hydrangea-like hollow nitrogen-rich carbon nanosheets remained unaffected by both Co ion incorporation and NH₄Cl low-temperature pyrolysis processes. HAADF-STEM characteriza-tion of Co-cluster/NC showed the extensive distribution of Co clusters on the NC substrate (Fig. S4†). This observation suggests that when the concentration of Co ions exceeds a critical threshold during adsorption, Co single atoms tend to aggregate into clusters, consequently diminishing the accessible surface area of catalytically active sites.

2.2 Electronic and coordination structures

The nitrogen adsorption–desorption isotherms and pore size analyses demonstrate the structural evolution promoted by NH₄Cl-assisted pyrolysis (Fig. 2). The initial NAP pyrolysis yielded a porous carbon framework with a surface area of 482.4 m² g⁻¹, which further increased to 644.3 m² g⁻¹ after NH₄Cl treatment and Co incorporation. The enhanced surface area can be attributed to the synergistic physical etching and chemical activation during NH₄Cl decomposition.[50] Notably, the generated acidic gas facilitates the formation of uniformly distributed Co–N₄ sites by reducing Co particles to ionic species and anchoring them at surface defects.[51,52] The resultant hierarchical mesoporous architecture (insets in Fig. 2a and b) provides efficient mass transport channels for O₂ and H⁺ diffusion, thereby optimizing the accessibility of active sites and enhancing the overall catalytic performance.[53]

Powder X-ray diffraction (XRD) patterns shown in Fig. 3a indicate the amorphous structure of the samples. The absence of cobalt monomers in Co-SAC/NC reveals that the cobalt atoms are highly dispersed throughout the NC material, with no larger aggregates present. XRD patterns of all four samples exclusively display two broad peaks attributed to the (002) and (100) crystallographic planes of graphite, corroborating the SAED patterns obtained from aberration-corrected HAADF-STEM analysis. Notably, the (002) diffraction peak exhibits a negative shift from about 26.6° (standard graphite) to approximately
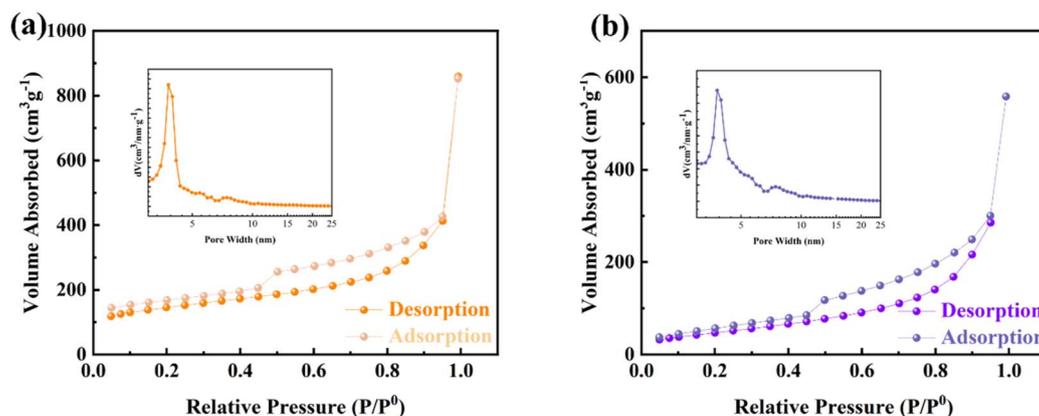

Fig. 2 Nitrogen adsorption–desorption isotherms and pore size distribution (inset in (a) and (b)) of the as-prepared catalysts (a) Co-SAC/NC and (b) NC.

This journal is © The Royal Society of Chemistry 2025

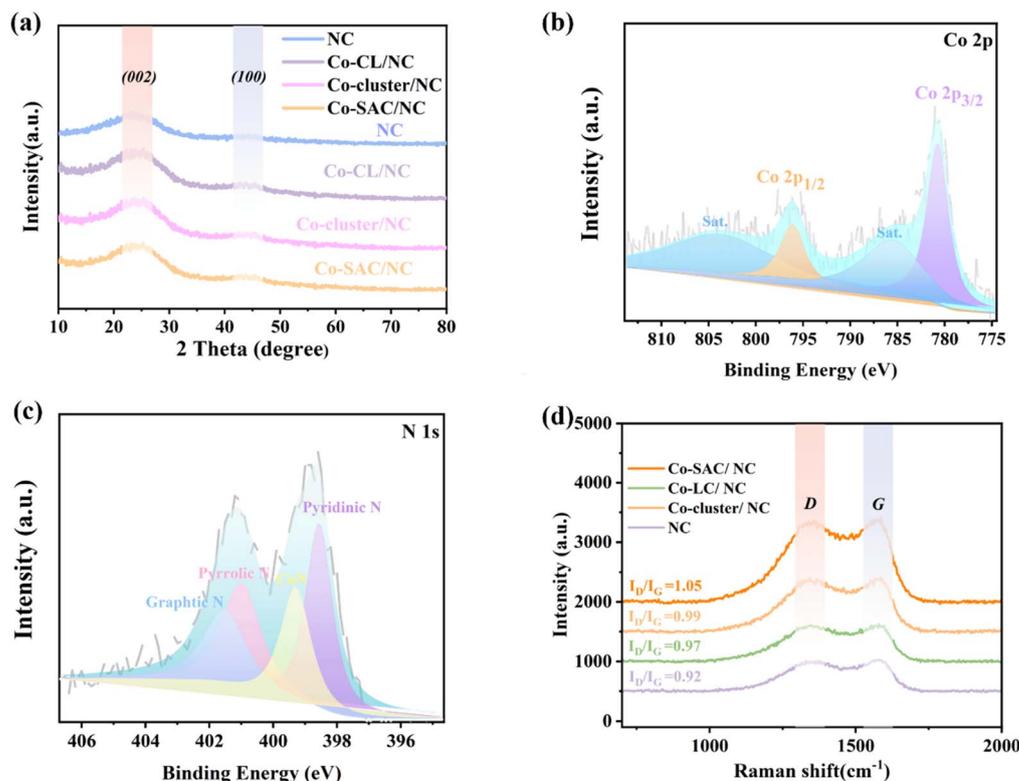*J. Mater. Chem. A*, 2025, **13**, 14631–14645 | **14633**

Fig. 3 Atomic structural analysis of Co-SAC/NC. (a) XRD patterns, high-resolution XPS of Co 2p, (b) and N 1s, (c) spectra, and (d) Raman spectra.

25.7°, demonstrating increased interlayer spacing resulting from substantial nitrogen incorporation. This structural modification is anticipated to enhance mass transport kinetics during electrochemical processes.[54]

X-ray photoelectron spectroscopy (XPS) analysis elucidated the chemical composition and electronic structure of Co-SAC/NC. The spectra exhibited distinct peaks corresponding to C, N, O, and Co elements (Fig. S5†). The Co 2p XPS spectrum of Co-SAC/NC was deconvoluted into two pair peaks, including Co–N spin–orbit coupling peaks (796 eV, Co $2p_{1/2}$ and 782 eV, Co $2p_{3/2}$) and two satellite peaks (Fig. 3b).[55] Previous studies have demonstrated that interactions between metal nanoparticles/clusters and metal–nitrogen (MN_x) sites typically result in alterations of charge density around the central metal atoms, leading to binding energy shifts in Co $2p_{3/2}$ and Co $2p_{1/2}$.[56,57] XPS analysis revealed no significant shifts in the Co $2p_{3/2}$ and Co $2p_{1/2}$ binding energies for Co-SAC/NC, corroborating the atomic dispersion of Co species and excluding the formation of Co nanoparticles.[58,59] In addition, XPS analysis further revealed the influence of Co adsorption on the compositional content and valence states of the samples. The high-resolution N 1s spectrum (Fig. 3c) was deconvoluted into four distinct peaks at 398.56, 399.29, 400.99, and 401.51 eV.[60–62] The peak at 400.99 eV is attributed to pyrrolic-N species, representing another form of CoN_4 active sites, while the peak at 401.51 eV is assigned to graphitic-N species.[62] The peak at 399.29 eV provides additional evidence for forming CoN_4 moieties.[63] A significant observation is the 0.17 eV negative shift in the pyridinic-N peak of the N 1s

spectra for Co-SAC/NC, Co-LC/NC, and Co-cluster/NC relative to pristine nitrogen-doped carbon (NC) (Fig. 3c and S6†).[55] This spectroscopic shift provides strong evidence for the formation of Co–N_4 coordination structures, resulting from the specific interaction between atomic Co and pyridinic-N moieties within the NC matrix.

As shown in Fig. S7,† all samples exhibited similar C 1s spectra and carbon content, suggesting a minimal impact of Co species introduction on the carbon structure. Analysis of the N 1s spectra revealed that with increasing Co adsorption, the pyridinic-N content decreased while the Co–N_x content increased. This can be attributed to the additional Co sources combined with pyridinic-N to form more abundant Co–N_x species, effectively promoting the ORR process.[64] Correspondingly, the cobalt content in the samples increased from 1.91 wt% to 4.12 wt% with increasing Co adsorption (Table S1†). Raman spectroscopic analysis reveals two prominent vibrational modes: a disorder-associated D-band centered at 1353 cm^{-1} and a graphitic G-band at 1588 cm^{-1}, elucidating the carbon material's microstructural characteristics.[65] The intensity ratio of D-band to G-band (I_D/I_G) serves as a quantitative indicator for structural defects in carbonaceous materials.[66] Raman spectroscopic analysis (Fig. 3d) reveals that the incorporation of cobalt at varying concentrations significantly modulates this ratio. Among the cobalt-modified catalysts, the I_D/I_G values exhibit a sequential variation, starting from 0.92 (NC) and increasing to 0.97 (Co-LC/NC) and 1.05 (Co-SAC/NC) before decreasing to 0.99 (Co-cluster/NC). The elevated I_D/I_G

14634 | J. Mater. Chem. A, 2025, 13, 14631–14645

This journal is © The Royal Society of Chemistry 2025

ratios observed in the carbonized products can be attributed to the condensation-induced formation of abundant defect edges along carbon boundaries.[67] This defect engineering process, facilitated by cobalt adsorption and NH$_4$Cl-mediated low-temperature pyrolysis, is crucial in enhancing the catalytic performance.

To elucidate the local electronic structure and coordination environment of cobalt species in Co-SAC/NC, comprehensive X-ray absorption spectroscopy was conducted and analyzed. Fig. 4a presents the Co K-edge X-ray absorption near-edge structure (XANES) spectra for Co-SAC/NC alongside relevant reference materials, including Co foil, Co$_3$O$_4$, cobalt phthalocyanine (CoPc), Co-cluster/NC, and CoO. These XANES profiles offer valuable insights into the oxidation state and local geometry of the cobalt atoms within the catalyst structure. Examination of the Co K-edge absorption threshold in Co-SAC/NC reveals its intermediate position relative to metallic cobalt and CoO references, implying a cobalt oxidation state between 0 and +2 in the catalyst.[55] Complementary structural information was obtained by analyzing the Fourier-transformed extended X-ray absorption fine structure (FT-EXAFS) data. The FT-EXAFS profiles for both Co-SAC/NC and Co-cluster/NC display a prominent feature at ca. 1.47 Å (Fig. 4b), offering crucial insights into the local coordination environment surrounding the cobalt centers.[68] This peak position is consistent with the Co–N coordination distance observed in cobalt phthalocyanine (CoPc, ≈1.47 Å), providing strong evidence for

Co–N coordination in the first shell environment of the cobalt centers. Additionally, the Co-cluster/NC sample exhibits an additional minor peak at 2.17 Å (Fig. S8†), consistent with the Co–Co bonding distance observed in Co foil (≈2.17 Å), which is consistent with the results of AC HAADF-STEM (Fig. S4†), providing direct spectroscopic evidence for the existence of Co clusters.[69]

Quantitative analysis of the local atomic structure surrounding cobalt species in Co-SAC/NC was conducted using least-squares EXAFS fitting. This analysis revealed the presence of isolated cobalt atoms coordinated with nitrogen, exhibiting a Co : N ratio of 4.1 ± 0.3 (Fig. 4c, d and Table S2†). To further corroborate these findings, wavelet transform (WT) analysis was applied to the EXAFS data. The resulting WT-EXAFS image (Fig. 4d) shows a maximum intensity at approximately $k = 1.47$ Å^{-1}, characteristic of Co–N coordination interactions. To further elucidate the local coordination environment, wavelet transform (WT) EXAFS analysis was conducted on multiple standard reference samples (Co foil, Co$_3$O$_4$, CoPc, and CoO) and Co-SAC/NC, enabling simultaneous resolution in both k- and R-space for backscattering atom discrimination.

The WT-EXAFS contour plot (Fig. 4e) reveals that Co-SAC/NC displays a distinct intense region centered at $k \approx 4.5$ Å^{-1} and $R \approx 1.4$ Å, which correlates excellently with the Co–N coordination features observed in the CoPc reference ($k = 4.5$ Å^{-1} and $R = 1.4$ Å).[12] The collective spectroscopic evidence substantiates the atomic-scale dispersion of cobalt within the Co-SAC/NC

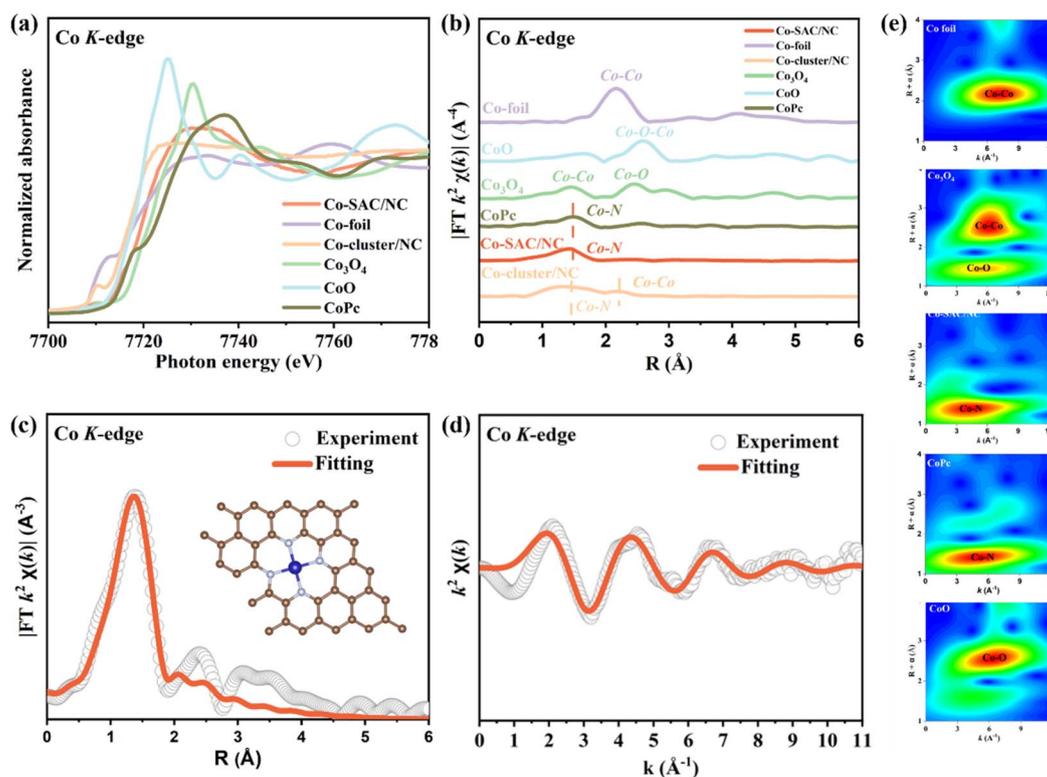

Fig. 4 Structural characterizations of Co-SAC/NC. (a) XANES spectra at Co K-edge and (b) K^3-weighted FT-EXAFS data of Co-SAC/NC, Co foil, Co$_3$O$_4$, CoPc, and CoO. (c) FT-EXAFS fitting patterns and (d) K^3-weighted Co K-edge EXAFS oscillations of Co-SAC/NC. (e) WT-EXAFS of Co foil, Co$_3$O$_4$, CoPc, CoO, and Co-SAC/NC.

This journal is © The Royal Society of Chemistry 2025

J. Mater. Chem. A, 2025, **13**, 14631–14645 | **14635**

material. These isolated cobalt atoms are uniformly distributed across the nitrogen-enriched carbon support, forming coordinated structures with nitrogen species. This interpretation aligns with the AC HAADF-STEM, as illustrated in Fig. 1f. In summary, the cumulative analytical evidence converges to confirm the predominant existence of cobalt as atomically dispersed species within the Co-SAC/NC framework.

2.3 Electrocatalytic ORR performance

The oxygen reduction reaction (ORR) performance of the synthesized catalysts was evaluated using a standard three-electrode configuration in an alkaline medium (0.1 M KOH). The electrocatalytic performance evaluation (Fig. 5a–c) revealed that Co-SAC/NC demonstrated remarkable catalytic activity, characterized by an outstanding half-wave potential ($E_{1/2}$) of 0.91 V *versus* RHE and a notably small Tafel slope of 62.54 mV dec^{-1}. These metrics substantially surpassed those of comparative systems, including Co-cluster/NC ($E_{1/2}$ = 0.87 V, Tafel slope = 92.73 mV dec^{-1}), Co-LC/NC ($E_{1/2}$ = 0.84 V, Tafel slope = 96.36 mV dec^{-1}), and pristine NC ($E_{1/2}$ = 0.69 V, Tafel slope = 141.61 mV dec^{-1}). Extraordinarily, Co-SAC/NC exhibited competitive performance against commercial Pt/C catalysts ($E_{1/}$

$_2$ = 0.86 V, Tafel slope = 83.62 mV dec^{-1}) and, as evidenced in Fig. 5f, outperformed the majority of previously reported Co-based single-atom electrocatalysts for ORR in the literature (Table S3†). In comparison, Co-SAC/NC exhibited the highest electrochemical performance, confirming the importance of the uniform distribution of Co single atoms, hollow porous structure, and the high density of Co–N_4 sites.

The synthesis strategy was systematically investigated by examining the influence of NH_4Cl concentration and thermal treatment conditions on the final catalyst structure. Various NH_4Cl loading ratios and pyrolysis temperatures were evaluated to determine their effects on material properties and catalytic performance. Building upon these optimization studies, the LSV curves in Fig. S10† provide compelling evidence for the critical roles of both NH_4Cl concentration and pyrolysis temperature. While the addition of NH_4Cl significantly enhanced the ORR activity initially, an interesting trend emerged: the catalytic performance at 100 mg NH_4Cl loading surpassed that of the 200 mg sample (Fig. S10a†). This unexpected behavior suggests a delicate balance in NH_4Cl optimization. The decreased performance with excessive NH_4Cl (200 mg) can be attributed to two potential mechanisms: (1) the generation of excess HCl during
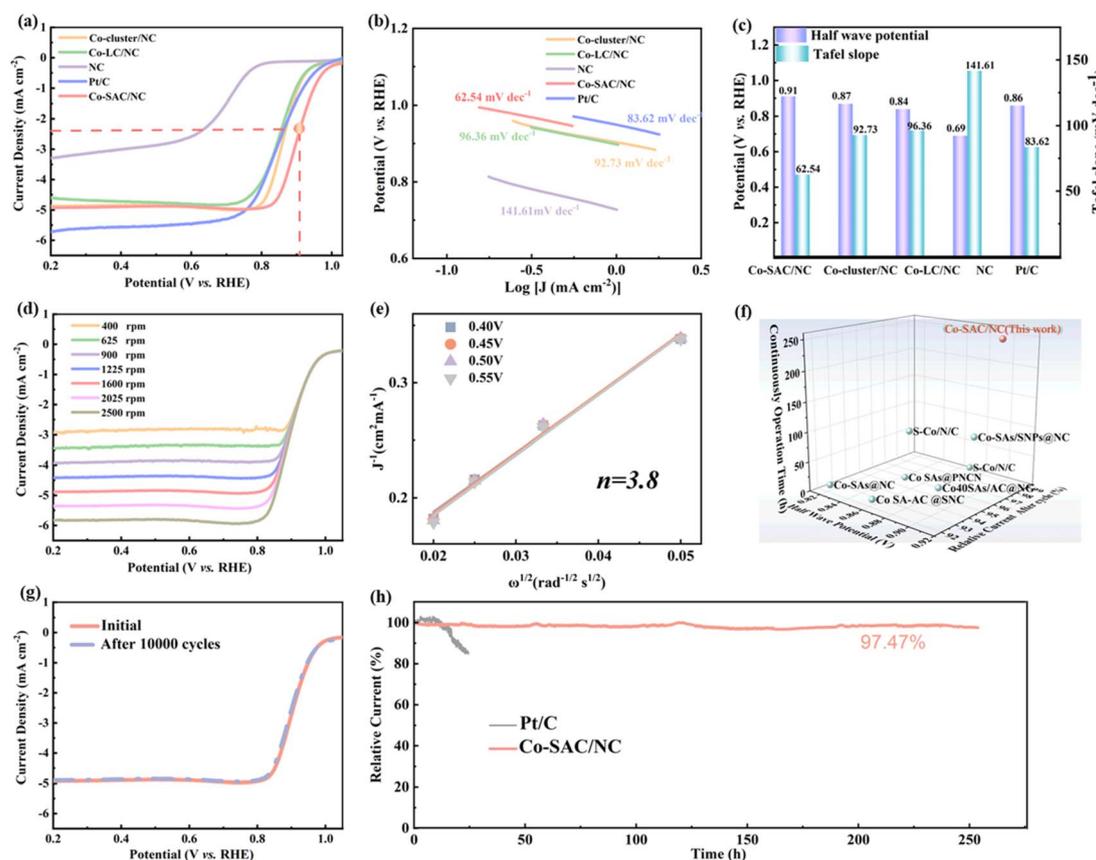

Fig. 5 Electrochemical ORR activity test. (a) LSV curves of Pt/C and the as-prepared catalysts. (b) The ORR Tafel plots for Pt/C and the as-prepared catalysts. (c) Half wave potential and Tafel slope values for Pt/C and the as-prepared catalysts. (d) Polarization curves of Co-SAC/NC at the rotating speed from 400 to 2500 rpm. (e) The responding K–L plots. (f) The half wave potential (V), relative current after cycle (%), and continuously operation time (h) of the Co-SAC/NC electrode, compared with the values of representative catalysts reported previously. (g) LSV curves of Co-SAC/NC before and after 10 000 CV cycles under the oxygen-saturated electrolyte at a scan rate of 5 mV s^{-1}. (h) Current density–time (*I*–*T*) curves of Pt/C and Co-SAC/NC.

14636 | *J. Mater. Chem. A*, 2025, **13**, 14631–14645

This journal is © The Royal Society of Chemistry 2025

thermal decomposition, which may compromise the material's structural integrity, and (2) the non-uniform decomposition of NH_4Cl at higher loadings, leading to inhomogeneous distribution of active sites. These findings underscore the importance of precise control over NH_4Cl concentration to achieve optimal catalytic performance through balanced formation of hierarchical porous structures and atomic Co–N_4 active sites while avoiding structural degradation. Furthermore, the pyrolysis temperature emerged as another crucial parameter influencing catalytic performance. While samples treated at 400 °C showed inferior performance due to incomplete NH_4Cl decomposition and residual chloride impurities, increasing the temperature to 500 °C led to optimal ORR activity (Fig. S10b†). However, further temperature elevation to 700 °C resulted in decreased performance. This non-monotonic temperature dependence can be rationalized as follows: at 400 °C, incomplete NH_4Cl decomposition leads to residual chloride contamination, compromising material purity and catalytic activity. When the temperature reaches 500 °C, optimal conditions are achieved, allowing for complete NH_4Cl decomposition, formation of uniform porous structures, preservation of high surface area, and well-defined Co–N_4 coordination environments (Fig. S9†). However, at 700 °C, excessive thermal treatment causes collapse of porous structures, reduction in specific surface area, and possible degradation of Co–N_4 active sites. This temperature-dependent behavior emphasizes the critical importance of precise thermal control during synthesis to achieve the optimal balance between complete precursor decomposition and structural integrity maintenance. The results clearly demonstrate that moderate temperature (500 °C) is most favorable for developing uniform porous structures and high surface area while maintaining the desired catalytic properties.

In order to evaluate the inherent catalytic performance of Co-SAC/NC, the electrochemically active surface area (ECSA) was examined and compared with previously reported catalysts. The ECSA calculations were based on measurements of the electrochemical double-layer capacitance (C_{dl}). Results showed that Co-SAC/NC demonstrated superior surface properties with a C_{dl} value reaching 72.1 mF cm^{-2}, corresponding to an ECSA of 1802.5 cm^2. These values substantially exceeded those of other reference materials (Table S4†), suggesting an enhanced availability of active sites for the ORR (Fig. S11†). The catalytic efficiency was evaluated through turnover frequency (TOF) calculations, incorporating parameters from ECSA measurements, BET surface area analysis, and catalyst loading data. Experimental results showed that the TOF values of Co-SAC/NC were markedly higher than those previously documented for other single-atom catalysts (Table S4†), indicating enhanced intrinsic catalytic capability of Co-SAC/NC active centers in the oxygen reduction reaction.

The reaction kinetics of all investigated catalysts were further evaluated through the Koutecky–Levich (K–L) analysis by plotting J^{-1} against $\omega^{-1/2}$ (Fig. 5d and e). Within the potential window of 0.40–0.55 V vs. RHE, the K–L plots exhibited excellent linearity with parallel slopes, suggesting first-order reaction kinetics in the ORR (cite). Quantitative analysis yielded an electron transfer number (n) of 3.8, indicating that the oxygen reduction proceeds predominantly through the desired four-electron transfer pathway rather than the less efficient two-electron process. Notably, the stability of the Co-SAC/NC catalyst was systematically evaluated through both accelerated durability testing (ADT) and chronoamperometric measurements, as illustrated in Fig. 5g and h. The ADT results demonstrated noteworthy stability after 10 000 consecutive CV cycles, with negligible degradation in the half-wave potential and minimal current decay (Fig. 5g). In the chronoamperometric test (Fig. 5h), the Co-SAC/NC catalyst exhibited superior durability compared to commercial Pt/C, showing negligible current attenuation after continuous operation for 253 h.

To further validate this exceptional stability, a comprehensive post-stability characterization of the catalyst's morphology and internal structure was conducted. SEM and TEM analyses (Fig. S12 and S13†) revealed that the Co-SAC/NC catalyst maintained its characteristic multi-layered graphene-like stacking structure without any apparent structural deterioration. The corresponding EDS mapping (Fig. S14†) confirmed the persistent uniform distribution of both N and Co elements throughout the porous carbon matrix. Most significantly, HAADF-STEM imaging (Fig. S15†) demonstrated that Co atoms remained atomically dispersed across the carbon substrate, with no evidence of Co nanoparticle or cluster formation, further substantiating the remarkable structural stability of the catalyst. Multiple synergistic structural and electronic factors can rationalize the superior ORR catalytic activity exhibited by Co-SAC/NC. First, the atomically dispersed Co sites achieve maximum atomic efficiency, providing numerous catalytically active centers for ORR. Second, the high concentration of nitrogen dopants, especially pyridinic N species, creates localized regions of enhanced positive charge density on adjacent carbon atoms. This optimizes O_2 adsorption kinetics and facilitates the subsequent ORR process.[70] Additionally, the hierarchical porous architecture of the ultrathin hollow carbon framework not only ensures efficient electron transfer and mass transport but also maximizes the exposure of active sites, collectively contributing to enhanced ORR performance.

2.4 DFT calculations

To elucidate the mechanistic underpinnings of the exceptional ORR activity exhibited by Co-SAC/NC, we employed spin-polarized density functional theory (DFT) calculations (Fig. 6a–d). The computational model was constructed based on the EXAFS fitting results, which indicated a predominant coordination environment of four nitrogen atoms surrounding each cobalt atom. Consequently, a Co–N_4–C structure was adopted as the foundation for our theoretical investigations. The optimized geometric configurations of O_2 molecules adsorbed on Co single-atom (Co-SAC/NC) and Co clusters (Co-cluster/NC) are depicted in Fig. 6b. The catalytic mechanism of isolated Co atoms in promoting ORR activity at CoN_4 active sites was thoroughly investigated through DFT calculations. At applied potentials of 0 V and 1.23 V, the third reaction step exhibits the highest free energy difference for CoN_4 sites in both Co-SAC/NC and Co-cluster/NC catalysts (Fig. 6a and S16†). This

This journal is © The Royal Society of Chemistry 2025

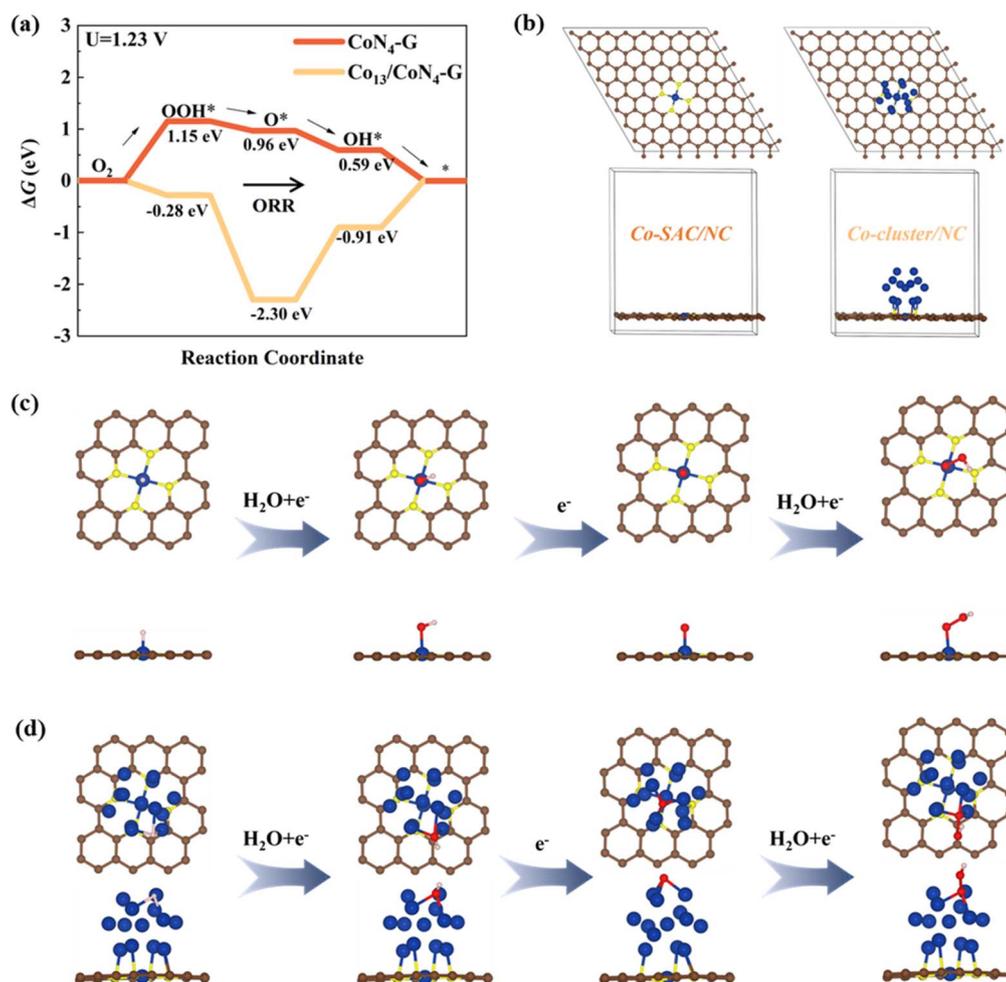*J. Mater. Chem. A*, 2025, **13**, 14631–14645 | **14637**

Fig. 6 (a) Calculated free energy diagrams of ORR at pH = 13 and U = 1.23 V for Co single atom and cluster anchoring. The inset shows the overpotential values. (b) Top-view and side-view of the adsorption geometries of OH* on CoN$_4$–C(Co-SAC/NC) and Co$_{13}$/CoN$_4$–C(Co-cluster/NC). Co, C, N, O, and H atoms are colored in blue, brown, yellow, red, and white, respectively (c) and (d) Schematic illustration of the 4e$^-$ pathway ORR process on Co–N$_4$active sites of Co-SAC/NC and Co-cluster/NC. The process involves the adsorption of O$_2$, the formation and transfer of oxygen-containing intermediates (Co–OOH, Co–O, and Co–OH) and the desorption of OH.

indicates that the desorption of O* (O* + H$^+$ + e$^-$ → OH*) from the active sites represents the potential-determining step, critically influencing the overall ORR kinetics.

Computational analysis of the Co–N$_4$–C structural motif revealed a remarkably low theoretical overpotential of 1.15 eV (Fig. 6a). This calculated value corroborates the experimentally observed high catalytic efficiency, underscoring the exceptional ORR performance of the system. The theoretical overpotential of Co$_{13}$/Co–N$_4$–C was calculated to be significantly higher (1.39 eV), indicating inferior ORR catalytic activity compared to the single-atomic Co–N$_4$–C active sites. This theoretical prediction aligns well with our experimental observations. The enhanced catalytic performance can be attributed to the uniform distribution of single-atomic catalytic sites on graphitic carbon, which maximizes the exposure of active sites. The catalytic cycle of the ORR for both Co–N$_4$–C and Co$_{13}$/Co–N$_4$–C systems is illustrated in Fig. 6c and d. Throughout this cycle, the cobalt atom undergoes dynamic repositioning, initially displaced from the graphene plane and

returning to its original position. This process is accompanied by significant alterations in both the geometric and electronic structures of the Co–N$_4$. The analysis reveals distinct spin-polarization states across various stages of the ORR process. The pristine Co–N$_4$ configuration exhibits a local magnetic moment of 0.96 μB on the cobalt atom. Upon forming the OOH* intermediate (Co–N$_4$ bound to OOH), this moment decreases to 0.48 μB. Interestingly, the O* configuration (Co–N$_4$ bound to O) demonstrates an enhanced magnetic moment of 2.61 μB on the cobalt center, with an additional moment of 0.50 μB observed on the adsorbed oxygen atom. This latter observation may be attributed to the partially filled p-orbital of the oxygen. In contrast, the OH* configuration (Co–N$_4$ bound to OH) presents a nearly quenched magnetic moment of 0.02 μB on the cobalt atom, indicating a transition to an unpolarized state. These findings underscore the complex interplay between structural dynamics and electronic reconfiguration in the Co–N$_4$ active site during the ORR process, providing valuable insights into the catalytic mechanism.

14638 | *J. Mater. Chem. A*, 2025, **13**, 14631–14645

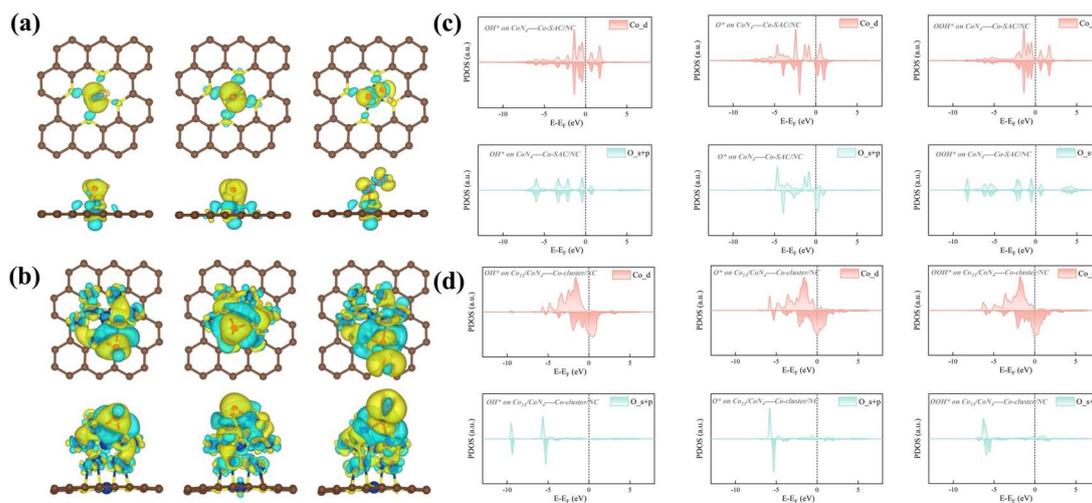This journal is © The Royal Society of Chemistry 2025

Fig. 7 Top-view and side-view of the charge density differences for OH*, O*, and OOH* on (a) Co-SAC/NC (b) Co-cluster/NC. Projected density of states (PDOS) of Co's d orbital and O's s + p orbitals for OH*, O*, and OOH* on (c) Co-SAC/NC and (d) Co-cluster/NC.

The charge density difference analysis presented in Fig. 7a and b further elucidates the localized nature of charge distribution in Co-SAC/NC, predominantly concentrated around the Co atomic active sites. This localization engenders an enhanced local electron density, which strengthens the interaction with oxygen molecules. Consequently, this electronic configuration reduces the activation energy for the ORR, thereby accelerating the reaction kinetics. Analysis of the projected density of states (PDOS) reveals distinct electronic configurations between single-atom (Fig. 7c) and cluster systems (Fig. 7d). In Co-SAC/NC, the OH* and OOH* intermediates exhibit symmetry between spin-up and spin-down states, indicating a balanced spin distribution. Conversely, the O* intermediate displays an asymmetric PDOS profile. This spin polarization in O* suggests a more complex electronic interaction with the single-atom active site. In contrast, the Co-cluster/NC system demonstrates asymmetric PDOS profiles across all intermediates (OH*, OOH*, and O*). This universal asymmetry implies a more pronounced spin polarization effect in the cluster configuration, potentially due to the collective electronic behavior of multiple metal atoms. These electronic structure differences between single-atom and cluster catalysts influence their respective catalytic performances, particularly in spin-sensitive reactions such as the ORR.

Analysis of the projected density of states (PDOS) reveals substantial orbital overlap between cobalt and oxygen in the energy range of −6 to 0 eV (Fig. S17 and S18†). This observation indicates robust hybridization between the d orbitals of cobalt and the s and p orbitals of oxygen. Such strong Co–O interactions likely play a pivotal role in driving both the geometric and electronic structural evolution throughout the ORR process. The decomposed atomic orbital magnetic moment (DAOMM) approach was employed to elucidate the origin of the observed magnetic moments. This method quantifies the difference in integrated PDOS between spin-up and spin-down channels at the Fermi level for specific atomic orbitals. The DAOMM analysis provides insights into the contribution of individual orbitals to the overall magnetic properties of the system. In the spin-unpolarized OH*

configuration, the decomposed atomic orbital magnetic moment (DAOMM) analysis reveals negligible contributions from all five d orbitals of the cobalt atom. Conversely, in the Co–N$_4$–C and OOH* systems, the d$_{z^2}$ orbital emerges as the primary contributor to the cobalt's magnetic moment, with DAOMM values of 0.83 μB and 0.44 μB, respectively. The O* system presents a more complex scenario, where all five d orbitals contribute significantly. DAOMM values range from 0.21 to 0.68 μB, culminating in a substantial local magnetic moment of 2.66 μB on the cobalt atom. These diverse spin states observed in the cobalt centers across different configurations underscore the profound influence of reactive intermediate species on the electronic structure of the Co–N$_4$–C active sites during the ORR process. Such electronic variability likely plays a crucial role in the catalytic mechanism, potentially contributing to the system's high ORR activity.

In summary, the asymmetric PDOS observed in O* for Co-SAC/NC indicates a controlled spin polarization, potentially optimizing the interaction with oxygen molecules. In contrast, the PDOS asymmetry in Co-cluster/NC systems might lead to excessive spin polarization, possibly hindering the balanced electron transfer required for efficient ORR. The controlled asymmetry observed in the O* PDOS for Co-SAC/NC might represent an optimized configuration for oxygen activation, a critical step in this ORR. The generalized asymmetry in Co-cluster/NC could lead to less effective oxygen activation, impacting the initiation of the reaction.

3. Conclusion

In this study, we have developed a novel approach for synthesizing a highly efficient ORR electrocatalyst. The method employs a low-temperature pyrolysis process involving NH$_4$Cl and metal ion adsorption, successfully anchoring isolated cobalt atoms onto defect-rich, nitrogen-doped carbon substrates. This innovative and accurate synthetic strategy yields a catalytic material with exceptional ORR performance. The hierarchical three-dimensional porous structure of Co-SAC/

This journal is © The Royal Society of Chemistry 2025

J. Mater. Chem. A, 2025, **13**, 14631–14645 | **14639**

NC exhibits dual functionality: enhancing mass transport efficiency while maximizing the exposure of atomically dispersed Co sites, which act as catalytically active centers for O_2 activation and transformation. The synthesized Co-SAC/NC catalyst demonstrates exceptional ORR performance and stability, surpassing many reported Co-based SACs. Theoretical simulations attribute this superior activity to the Co–N_4 moiety and elucidate the evolution of the Co sites' electronic structure, stemming from robust Co–O interactions during the ORR process. This study integrates experimental and computational approaches, offering both an innovative, highly efficient synthesis strategy and novel insights into the rational design of high-performance SACs.

4. Experimental section

4.1 Preparation

4.1.1 Chemicals. Cobalt(II) chloride hexahydrate ($CoCl_2 \cdot 6H_2O$), NH_4Cl, and methanol were purchased from Fisher Scientific. 2-Methylimidazole (2-MIM), 5-aminotetrazole (5-AT) and $Zn(CH_3COO)_2 \cdot 2H_2O$ were purchased from Sigma-Aldrich.

4.1.2 Synthesis of novel assembled precursor (NAP). An ordinary synthesis involved dissolving 1.455 g of $Zn(CH_3COO)_2 \cdot 2H_2O$, 0.38 g 5-aminotetrazole (5-AT), and 1.642 g of 2-methyl imidazole in 80 mL of methanol, respectively. After combining the two solutions above, the mixture was left at room temperature for 30 minutes while agitated. Centrifugation at 11 000 rpm for two minutes was used to separate the product, which was then cleaned several times with ethanol. A vacuum oven was used to dry the NAP powder overnight.

4.1.3 Synthesis of NC. The NAP precursor was thermally treated by placing it in a porcelain boat and heating it to 800 °C for 4 h under an inert N_2 atmosphere. After natural cooling to ambient temperature, the as-obtained black product underwent acid treatment in a 1 M HCl solution (200 mL) for 48 h to remove unstable species. This was followed by thorough washing with distilled water and subsequent drying at 70 °C.

4.1.4 Synthesis of Co-SAC/NC. The synthesis procedure involved the dispersion of $CoCl_2 \cdot 6H_2O$ ethanol solution (50 μL, containing 0.2 mg Co^{2+}) onto the NC substrate (10 mg). The obtained solid was homogeneously mixed with NH_4Cl (100 mg) after solvent evaporation. The resultant mixture underwent thermal annealing at 500 °C for 2 h in an Ar atmosphere.

4.1.5 Synthesis of Co-cluster/NC. To prepare Co-cluster/NC, the dispersion of $CoCl_2 \cdot 6H_2O$ ethanol solution (50 μL, containing 0.4 mg Co^{2+}) onto the NC substrate (10 mg).

4.1.6 Synthesis of Co-LC/NC. To prepare Co-LC/NC, the dispersion of $CoCl_2 \cdot 6H_2O$ ethanol solution (50 μL, containing 0.1 mg Co^{2+}) onto the NC substrate (10 mg).

4.1.7 Synthesis of Co-SAC/NC (200 mg NH_4Cl). The synthesis procedure involved the dispersion of $CoCl_2 \cdot 6H_2O$ ethanol solution (50 μL, containing 0.4 mg Co^{2+}) onto the NC substrate (20 mg). Following solvent evaporation, the obtained solid was homogeneously mixed with NH_4Cl (100 mg). The resultant mixture underwent thermal annealing at 500 °C for 2 h in an Ar atmosphere.

4.1.8 Synthesis of Co-SAC/NC (50 mg NH_4Cl). The synthesis procedure involved the dispersion of $CoCl_2 \cdot 6H_2O$ ethanol solution (50 μL, containing 0.4 mg Co^{2+}) onto the NC substrate (10 mg). Following solvent evaporation, the obtained solid was homogeneously mixed with NH_4Cl (100 mg). The resultant mixture underwent thermal annealing at 500 °C for 2 h in an Ar atmosphere.

4.1.9 Synthesis of Co-SAC/NC (0 mg NH_4Cl). The synthesis procedure involved the dispersion of $CoCl_2 \cdot 6H_2O$ ethanol solution (50 μL, containing 0.4 mg Co^{2+}) onto the NC substrate (10 mg). Following solvent evaporation, the obtained solid was homogeneously mixed with NH_4Cl (100 mg). The resultant mixture underwent thermal annealing at 500 °C for 2 h in an Ar atmosphere.

4.1.10 Co-SAC/NC (NH_4Cl at 700 °C). The synthesis procedure involved the dispersion of $CoCl_2 \cdot 6H_2O$ ethanol solution (50 μL, containing 0.4 mg Co^{2+}) onto the NC substrate (10 mg). Following solvent evaporation, the obtained solid was homogeneously mixed with NH_4Cl (100 mg). The resultant mixture underwent thermal annealing at 700 °C for 2 h in an Ar atmosphere.

4.1.11 Co-SAC/NC (NH_4Cl at 400 °C). The synthesis procedure involved the dispersion of $CoCl_2 \cdot 6H_2O$ ethanol solution (50 μL, containing 0.4 mg Co^{2+}) onto the NC substrate (10 mg). Following solvent evaporation, the obtained solid was homogeneously mixed with NH_4Cl (100 mg). The resultant mixture underwent thermal annealing at 400 °C for 2 h in an Ar atmosphere.

4.2 Characterization

Microstructural and morphological analyses were conducted using a Zeiss Sigma field-emission scanning electron microscope (FESEM) at 5 kV. Transmission electron microscopy (TEM), high-resolution TEM (HR-TEM), and elemental mapping were performed on a JEM-ARM200CF microscope equipped with an energy dispersive spectrometer (EDS), operating at 200 kV with EDS capabilities up to 300 kV. X-ray diffraction (XRD) patterns were obtained using a Rigaku Ultima IV diffractometer with Cu Kα radiation ($\lambda = 1.54056$ Å). X-ray photoelectron spectroscopy (XPS) measurements employed a Kratos Axis Ultra spectrometer with an Al Kα X-ray source. Metal content quantification was achieved via inductively coupled plasma optical emission spectroscopy (ICP-OES) using an Agilent 5110 system. Specific surface area and pore size distribution were determined through N_2 physisorption experiments on a Quantachrome Autosorb-IQ analyzer, utilizing the Brunauer–Emmett–Teller (BET) method and Barrett–Joyner–Halenda (BJH) model, respectively. X-ray absorption fine structure (XAFS) spectra were acquired at the Canadian light source synchrotron facility. Subsequently, X-ray absorption near edge structure (XANES) and extended X-ray absorption fine structure (EXAFS) data were processed using Athena software.

4.3 Electrochemical measurements

Electrocatalytic ORR testing was performed using a Biologic VMP-3 electrochemical workstation. The three-electrode system comprised a graphite rod counter electrode, a saturated calomel

electrode (SCE) reference, and a sample-coated glassy carbon working electrode. Catalyst slurry was prepared by ultrasonically dispersing 4 mg of sample in 400 μL of 0.5 wt% Nafion isopropanol-ethanol solution for two hours. The working electrode (5 mm diameter) was fabricated by depositing 6.5 μL of this ink. ORR activity was evaluated through linear sweep voltammetry (LSV), scanning from −1.0 V to 0 V (*vs.* SCE) at 5 mV s^{-1} with a rotation rate of 1600 rpm. Tafel slopes were derived from LSV curves using the equation $\eta = b \log j$. Catalyst stability was assessed *via* chronoamperometric measurements conducted at the overpotential corresponding to the half-wave potential.

The capacitive currents of $\Delta J = (J_a - J_c)/2$ are plotted as a function of the scan rate. The slope of the fitting line is equal to C_{dl}. The following formula was used to calculate the ECSA (ECSA = C_{dl}/C_s). For a flat surface, the specific capacitance (C_s) of 40 μF cm^{-2} was used here for the calculation of ECSA.

In this work, the TOF values are determined by the current density (j) for H$_2$O production normalized by ECSA (A cm^{-2}), the geometrical surface area of the working electrode (S, cm^2) and the number of active sites ($N_{active\ sites}$) according to the following equation:

$$TOF(\text{electron per site per s}) = \frac{j \times S}{n \times F \times N_{active\ sites}/NA}$$

where n is the number of electrons transferred to generate one molecule of the H$_2$O, F is the faradaic constant (96 485 C mol^{-1}), NA is the Avogadro constant (6.022 × 1023 mol^{-1}).

$$N_{active\ sites} = S_{BET} \times m_{loading} \times D_{atom} \times W_{site}$$

where S_{BET} is the BET surface area (m^2 g^{-1}), D_{atom} is a constant of carbon atomic density in graphene layer (3.82 × 10^{15} atoms cm^{-2}), W_{site} is the atomic percentage of active sites in the catalyst measured by ICP (it assumes that all the Sn sites were exposed and acted as the active sites for ORR), $m_{loading}$ is the mass of catalyst loading on the working electrode (mg).
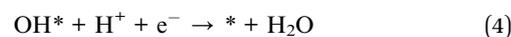
4.4 Computational methods

The first-principles calculations based on the density functional theory (DFT) were performed using the Vienna *ab initio* simulation package (VASP).[71–73] Electronic exchange-correlation effects were modeled within the generalized gradient approximation (GGA) by the Perdew–Burke–Ernzerhof (PBE) functional.[74] The electron–ion interactions were represented by the projector augmented wave (PAW) pseudopotentials[75,76] with the C-2s22p2, N-2s22p3, O-2s22p4, H-1s1, and Co-3d84s1 treated as valence electrons. The energy cutoff for the plane-wave expansion was 500 eV, and the DFT dispersion correlation method (DFT-D3) proposed by Grimme[77] was used to treat the van der Waals interactions. The Gaussian method was employed for the Fermi surface smearing with a width of 0.1 eV to improve the self-consistent convergence. Spin polarization was included to consider magnetic effects.

With these specifications, the lattice parameter of bulk graphite was predicted to be 2.464 Å, which is in good agreement with the experimental value (2.461 Å[78]) and the published

DFT result (2.464 Å[79]). Based on the optimized bulk structure, the slab model of a (8 × 8) graphene sheet was constructed and employed to build the Co and N codoped graphene system (CoN$_4$-G), in which Co atom substitutes two neighboring C atoms and four N atoms were introduced to replace the C atoms around Co (Fig. 1a). An additional vacuum layer of 18 Å was established along the direction perpendicular to the slab to avoid the interaction between the upper and lower surfaces due to periodic boundary conditions. An icosahedral Co$_{13}$ cluster was placed on CoN$_4$ doped graphene (Co$_{13}$/CoN$_4$-G) to mimic the catalyst substrate with a high concentration of Co (Fig. 1b). The k-point mesh of 3 × 3 × 1 was generated using the Monkhorst–Pack scheme[80] to sample the Brillouin zone. To obtain the most stable adsorption geometries of OH, O, and OOH on catalyst substrates, ion relaxations were performed using the standard conjugate-gradient method with a force truncation criterium of 0.02 eV Å^{-1}.

For ORR, the reaction process involves four-electron transfer steps on the surface:[81]

$$* + O_2 + H^+ + e^- \rightarrow OOH^* \tag{1}$$

$$OOH^* + H^+ + e^- \rightarrow O^* + H_2O \tag{2}$$

$$O^* + H^+ + e^- \rightarrow OH^* \tag{3}$$

$$OH^* + H^+ + e^- \rightarrow * + H_2O \tag{4}$$

where the * represents an adsorption site on the surface. The adsorption energies of the oxygen-containing intermediates were calculated by following equations:[81]

$$\Delta E_{OH^*} = E_{OH^*} - E^* - (E_{H_2O} - 1/2E_{H_2}) \tag{5}$$

$$\Delta E_{O^*} = E_{O^*} - E^* - (E_{H_2O} - E_{H_2}) \tag{6}$$

$$\Delta E_{OOH^*} = E_{OOH^*} - E^* - (2E_{H_2O} - 3/2E_{H_2}) \tag{7}$$

where E^* represents the total energy of the pure surface; E_{OH^*}, E_{O^*}, and E_{OOH^*} are the total energies of the systems with absorbates OH, O, and OOH, respectively. E_{H_2O} and E_{H_2} denote the total energies of free H$_2$O and H$_2$ molecules, respectively. The adsorption free energies can be obtained by including the zero-point energy (ZPE) and the entropy (S) corrections in equation

$$\Delta G_{ads} = \Delta E_{ads} + \Delta ZPE - T\Delta S \tag{8}$$

ΔZPE and $T\Delta S$ can be obtained from vibrational frequency calculations and standard tables for the reactants and products in the gas phase.[82,83] Then, the change of free energy during the chemical reaction can be obtained from the following:

$$\Delta G = \Delta G_{ads} + \Delta G_U + \Delta G_{pH} \tag{9}$$

ΔG_U and ΔG_{pH} the free energy contributions due to variations in electrode potential U and the pH value, respectively. $\Delta G_U = -neU$, where n is the number of electrons transferred. $\Delta G_{pH} = -k_BT\ln[H^+] = pH \times k_BT \times \ln 10$, where k_B is the Boltzmann

This journal is © The Royal Society of Chemistry 2025

J. Mater. Chem. A, 2025, **13**, 14631–14645 | **14641**

constant. In this work, we set pH to 13 and T to 300 K, respectively.

The charge density differences at the adsorption interfaces were evaluated using the expression:

$$\Delta\rho(r) = \rho_{X*}(r) - \rho^*(r) - \rho_X(r) \qquad (10)$$

where $\rho_{X*}(r)$, $\rho^*(r)$, and $\rho_X(r)$ are the charge densities of the adsorbate/surface system, the pure surface, and the isolated X molecule, respectively. The projected density of states (PDOS) was plotted using the post-processing VASPKIT package.[84]

Data availability

The authors confirm that the data supporting the findings of this study are available within the article and its ESI.†

Author contributions

Ge Li: conceptualization; funding acquisition, project administration, resources, supervision, writing – review & editing. Xiaolan Gao: conceptualization, methodology, data curation, formal analysis, software, visualization; writing – original draft preparation. Yue Li: calculation, software, writing – review. Zhiqing Zhang: methodology, formal analysis, software, visualization. Hao Zhang: methodology, formal analysis, software, visualization.

Conflicts of interest

The authors declare that the research was conducted without any commercial or financial relationships that could be construed as a potential conflict of interest.

Acknowledgements

References

1 C. Baik, S. W. Lee and C. Pak, Control of the pore size distribution inside the RuO2 catalyst by using silica nanosphere particle for highly efficient water electrolysis, *Microporous Mesoporous Mater.*, 2020, **309**, 110567.

2 Z. Deng, A. H. B. Mostaghimi, M. Gong, N. Chen, S. Siahrostami and X. Wang, Pd 4d orbital overlapping modulation on Au@ Pd nanowires for efficient H_2O_2 production, *J. Am. Chem. Soc.*, 2024, **146**(4), 2816–2823.

3 J. Zong, C. He and W. Zhang, Ultrafast carrier recombination in a BC 6 N/SnXY Z-scheme heterostructure for water splitting: insights from ground-and excited-state carrier dynamics, *J. Mater. Chem. A*, 2024, **12**(29), 18528–18536.

4 W. Zhang, X. He and C. He, The "dp orbital hybridization"-guided design of novel two-dimensional MOFs with high anchoring and catalytic capacities in Lithium– Sulfur batteries, *J. Colloid Interface Sci.*, 2025, **678**, 540–548.

5 Z. Chen, S. Yun, L. Wu, J. Zhang, X. Shi, W. Wei, Y. Liu, R. Zheng, N. Han and B.-J. Ni, Waste-derived catalysts for water electrolysis: circular economy-driven sustainable green hydrogen energy, *Nano-Micro Lett.*, 2022, **15**(1), 4.

6 M. Gong, D. Xiao, Z. Deng, R. Zhang, W. Xia, T. Zhao, X. Liu, T. Shen, Y. Hu and Y. Lu, Structure evolution of PtCu nanoframes from disordered to ordered for the oxygen reduction reaction, *Appl. Catal., B*, 2021, **282**, 119617.

7 Y.-T. Zhang, F. Zhang, Z. Lu, J.-M. Luo, S.-Y. Feng, Q. Wang, H. Chen, H.-M. Wu, Z.-P. Miao and B. Chi, CrN supported by carbon nanosheets as efficient catalysts toward oxygen reduction reaction and Zn-air batteries, *Rare Metals*, 2024, **43**(10), 4973–4981.

8 W. Zhang, S. Kong, W. Wang, Y. Cheng, Z. Li and C. He, Enhanced electrocatalytic performance of LCO-NiFe-C3N4 composite material for highly efficient overall water splitting, *J. Colloid Interface Sci.*, 2025, **680**, 787–796.

9 Z. Deng, S. Jin, M. Gong, N. Chen, W. Chen, M. H. Seo and X. Wang, Potential-driven coordinated oxygen migration in an electrocatalyst for sustainable H_2O_2 synthesis, *ACS Nano*, 2024, **18**(47), 32834–32846.

10 Z. Deng, Z. Gong, M. Gong and X. Wang, Multiscale regulation of ordered PtCu intermetallic electrocatalyst for highly durable oxygen reduction reaction, *Nano Lett.*, 2024, **24**(13), 3994–4001.

11 C. Lai, M. Gong, Y. Zhou, J. Fang, L. Huang, Z. Deng, X. Liu, T. Zhao, R. Lin and K. Wang, Sulphur modulated Ni3FeN supported on N/S co-doped graphene boosts rechargeable/ flexible Zn-air battery performance, *Appl. Catal., B*, 2020, **274**, 119086.

12 W. Song, C. Xiao, J. Ding, Z. Huang, X. Yang, T. Zhang, D. Mitlin and W. Hu, Review of carbon support coordination environments for single metal atom electrocatalysts (SACS), *Adv. Mater.*, 2024, **36**(1), 2301477.

13 Z. Zhang, C. Qiao, J. Li, P. Li, H. Zhang, Q. Liu, H. Zeng and G. Li, Weakened hydrophobic interactions enhance bubble release in electrocatalytic water-splitting, *Appl. Catal., B*, 2025, 125019.

14 Y. Yu, P. Rao, S. Feng, M. Chen, P. Deng, J. Li, Z. Miao, Z. Kang, Y. Shen and X. Tian, Atomic Co clusters for efficient oxygen reduction reaction, *Acta Phys.-Chim. Sin.*, 2023, **39**, 2210039.

15 C. Wu, Y. Yu, Y. Song, P. Rao, X. Han, Y. Liang, J. Li, K. Zhang, Z. Zhang and P. Deng, Pyrrole-type TM-N3 sites as high-efficient bifunctional oxygen reactions electrocatalysts: from theoretical prediction to experimental validation, *J. Energy Chem.*, 2025, **104**, 472–481.

16 M. Gong, Z. Deng, D. Xiao, L. Han, T. Zhao, Y. Lu, T. Shen, X. Liu, R. Lin, T. Huang, G. Zhou, H. Xin and D. Wang, One-nanometer-thick PT_3Ni bimetallic alloy nanowires advanced oxygen reduction reaction: integrating multiple

14642 | *J. Mater. Chem. A*, 2025, **13**, 14631–14645

This journal is © The Royal Society of Chemistry 2025

advantages into one catalyst, *ACS Catal.*, 2019, **9**(5), 4488–4494.

17 Y. Guo, T. Park, J. W. Yi, J. Henzie, J. Kim, Z. Wang, B. Jiang, Y. Bando, Y. Sugahara and J. Tang, Nanoarchitectonics for transition-metal-sulfide-based electrocatalysts for water splitting, *Adv. Mater.*, 2019, **31**(17), 1807134.

18 L. Yang, C. Du, J. Tian, X. Yao, Q. Zhang, X. Ma, Y. Zhu, M. Zou and C. Cao, Fully exposed copper single-atom sites on mesoporous N/S-codoped graphene for efficient zinc-air battery, *Appl. Catal., B*, 2024, **355**, 124190.

19 V. Hasija, A. Kumar, A. Sudhaik, P. Raizada, P. Singh, Q. Van Le, T. T. Le and V.-H. Nguyen, Step-scheme heterojunction photocatalysts for solar energy, water splitting, CO_2 conversion, and bacterial inactivation: a review, *Environ. Chem. Lett.*, 2021, **19**(4), 2941–2966.

20 L. R. Jabbar and A. Al-Farraji, S-scheme ZIF-8/Ag2S heterojunction photocatalyst for degradation of organic pollutant using batch and external loop airlift reactors, *Environ. Nanotechnol. Monitor. Manage.*, 2022, **18**, 100701.

21 H. S. Jadhav, H. A. Bandal, S. Ramakrishna and H. Kim, Critical review, recent updates on zeolitic imidazolate framework-67 (ZIF-67) and its derivatives for electrochemical water splitting, *Adv. Mater.*, 2022, **34**(11), 2107072.

22 Z. Li, S. Ji, C. Xu, L. Leng, H. Liu, J. H. Horton, L. Du, J. Gao, C. He and X. Qi, Engineering the electronic structure of single-atom iron sites with boosted oxygen bifunctional activity for zinc–air batteries, *Adv. Mater.*, 2023, **35**(9), 2209644.

23 H. Yang, Z. Chen, W. Hao, H. Xu, Y. Guo and R. Wu, Catalyzing overall water splitting at an ultralow cell voltage of 1.42 V *via* coupled Co-doped NiO nanosheets with carbon, *Appl. Catal., B*, 2019, **252**, 214–221.

24 J. Yu, Y. Dai, Q. He, D. Zhao, Z. Shao and M. Ni, A mini-review of noble-metal-free electrocatalysts for overall water splitting in non-alkaline electrolytes, *Mater. Rep. Energy*, 2021, **1**(2), 100024.

25 Z. Lv, Z. Shu, J. Luo, J. Xu, Y. Ma, L. Zhang, H. Xu and Z. Mao, Asymmetric high-coordination Co-NSP single-atom catalysts with tailored dp-orbital electron structure for efficient bifunctional catalyst of rechargeable Zn-air battery cathodes, *Appl. Catal., B*, 2025, **365**, 124889.

26 H. Yuan, S. Wang, Z. Ma, M. Kundu, B. Tang, J. Li and X. Wang, Oxygen vacancies engineered self-supported B doped Co3O4 nanowires as an efficient multifunctional catalyst for electrochemical water splitting and hydrolysis of sodium borohydride, *Chem. Eng. J.*, 2021, **404**, 126474.

27 X. Yuan, J. Yin, Z. Liu, X. Wang, C. Dong, W. Dong, M. S. Riaz, Z. Zhang, M.-Y. Chen and F. Huang, Charge-transfer-promoted high oxygen evolution activity of Co@Co9S8 core-shell nanochains, *ACS Appl. Mater. Interfaces*, 2018, **10**(14), 11565–11571.

28 C. Zhong, Z. Han, T. Wang, Q. Wang, Z. Shen, Q. Zhou, J. Wang, S. Zhang, X. Jin and S. Li, Aliovalent fluorine doping and anodization-induced amorphization enable bifunctional catalysts for efficient water splitting, *J. Mater. Chem. A*, 2020, **8**(21), 10831–10838.

29 C. Zhu, A.-L. Wang, W. Xiao, D. Chao, X. Zhang, N. H. Tiep, S. Chen, J. Kang, X. Wang, J. Ding, J. Wang, H. Zhang and H. J. Fan, *In situ* grown epitaxial heterojunction exhibits high-performance electrocatalytic water splitting, *Adv. Mater.*, 2018, **30**(13), 1705516.

30 G. Zhuang, Q. Fang, J. Wei, C. Yang, M. Chen, Z. Lyu, Z. Zhuang and Y. Yu, Branched In2O3 mesocrystal of ordered architecture derived from the oriented alignment of a metal–organic framework for accelerated hydrogen evolution over In2O3–ZnIn2S4, *ACS Appl. Mater. Interfaces*, 2021, **13**(8), 9804–9813.

31 Y. Yang, Y. Xiao, L. Zhang, H.-T. Wang, K.-H. Chen, W.-X. Lin, N. Jin, C. Sun, Y.-C. Shao and J.-L. Chen, Encaging Co nanoparticle in atomic CoN4-dispersed graphite nanopocket evokes high oxygen reduction activity for flexible Zn-air battery, *Appl. Catal., B*, 2024, **347**, 123792.

32 X.-P. Li, C. Huang, W.-K. Han, T. Ouyang and Z.-Q. Liu, Transition metal-based electrocatalysts for overall water splitting, *Chin. Chem. Lett.*, 2021, **32**(9), 2597–2616.

33 Z. Li, M. Hu, P. Wang, J. Liu, J. Yao and C. Li, Heterojunction catalyst in electrocatalytic water splitting, *Coord. Chem. Rev.*, 2021, **439**, 213953.

34 Z. Li, B. Li, C. Yu, H. Wang and Q. Li, Recent progress of hollow carbon nanocages: general design fundamentals and diversified electrochemical applications, *Adv. Sci.*, 2023, 2206605.

35 Y. Lin, Y. Pan, S. Liu, K. Sun, Y. Cheng, M. Liu, Z. Wang, X. Li and J. Zhang, Construction of multi-dimensional core/shell Ni/NiCoP nano-heterojunction for efficient electrocatalytic water splitting, *Appl. Catal., B*, 2019, **259**, 118039.

36 H. Liu, J. Gao, X. Xu, Q. Jia, L. Yang, S. Wang and D. Cao, Oriented construction Cu3P and Ni2P heterojunction to boost overall water splitting, *Chem. Eng. J.*, 2022, **448**, 137706.

37 J. M. V. Nsanzimana, Y. Peng, Y. Y. Xu, L. Thia, C. Wang, B. Y. Xia and X. Wang, An efficient and earth-abundant oxygen-evolving electrocatalyst based on amorphous metal borides, *Adv. Energy Mater.*, 2018, **8**(1), 1701475.

38 L. Pei, Y. Song, M. Song, P. Liu, H. Wei, B. Xu, J. Guo and J. Liang, Mo-doping induced edge-rich cobalt iron oxide ultrathin nanomeshes as efficient bifunctional electrocatalysts for overall water splitting, *Electrochim. Acta*, 2021, **368**, 137651.

39 H. Sun, Z. Yan, F. Liu, W. Xu, F. Cheng and J. Chen, Self-supported transition-metal-based electrocatalysts for hydrogen and oxygen evolution, *Adv Mater.*, 2020, **32**(3), 1806326.

40 Y. Sun, T. Zhang, C. Li, K. Xu and Y. Li, Compositional engineering of sulfides, phosphides, carbides, nitrides, oxides, and hydroxides for water splitting, *J. Mater. Chem. A*, 2020, **8**(27), 13415–13436.

41 I. Ullah, A. Munir, A. Haider, N. Ullah and I. Hussain, Supported polyoxometalates as emerging nanohybrid materials for photochemical and photoelectrochemical water splitting, *Nanophotonics*, 2021, **10**(6), 1595–1620.

42 J. Wang, J. Hu, C. Liang, L. Chang, Y. Du, X. Han, J. Sun and P. Xu, Surface reconstruction of phosphorus-doped cobalt

This journal is © The Royal Society of Chemistry 2025

J. Mater. Chem. A, 2025, **13**, 14631–14645 | **14643**

molybdate microarrays in electrochemical water splitting, *Chem. Eng. J.*, 2022, **446**, 137094.

43 M. Wang, L. Zhang, Y. He and H. Zhu, Recent advances in transition-metal-sulfide-based bifunctional electrocatalysts for overall water splitting, *J. Mater. Chem. A*, 2021, **9**(9), 5320–5363.

44 Z. Deng, M. Gong, Z. Gong and X. Wang, Mesoscale mass transport enhancement on well-defined porous carbon platform for electrochemical H_2O_2 synthesis, *Nano Lett.*, 2022, **22**(23), 9551–9558.

45 Z. Wang, H. Liu, R. Ge, X. Ren, J. Ren, D. Yang, L. Zhang and X. Sun, Phosphorus-doped Co_3O_4 nanowire array: a highly efficient bifunctional electrocatalyst for overall water splitting, *ACS Catal.*, 2018, **8**(3), 2236–2241.

46 Q. Wen, K. Yang, D. Huang, G. Cheng, X. Ai, Y. Liu, J. Fang, H. Li, L. Yu and T. Zhai, Schottky heterojunction nanosheet array achieving high-current-density oxygen evolution for industrial water splitting electrolyzers, *Adv. Energy Mater.*, 2021, **11**(46), 2102353.

47 D. Yan, R. Chen, Z. Xiao and S. Wang, Engineering the electronic structure of Co_3O_4 by carbon-doping for efficient overall water splitting, *Electrochim. Acta*, 2019, **303**, 316–322.

48 J. Yan, F. Ye, Q. Dai, X. Ma, Z. Fang, L. Dai and C. Hu, Recent progress in carbon-based electrochemical catalysts: from structure design to potential applications, *Nano Res. Energy*, 2023, **2**(2), e9120047.

49 Z. Wang, Y. Zeng, J. Deng, Z. Wang, Z. Guo, Y. Yang, X. Xu, B. Song, G. Zeng and C. Zhou, Preparation and application of single-atom cobalt catalysts in organic synthesis and environmental remediation, *Small Methods*, 2024, **8**(3), 2301363.

50 Z. Wu, K. Zhang, C. Ma, S. Luo, W. Li and S. Liu, Synthesis of nitrogen-doped hierarchically porous carbons with ordered mesopores from liquefied wood: pore architecture manipulation by NH_4Cl for improved electrochemical performance, *J. Energy Storage*, 2023, **68**, 107619.

51 D. Ping, F. Yi, G. Zhang, S. Wu, S. Fang, K. Hu, B. B. Xu, J. Ren and Z. Guo, NH4Cl-assisted preparation of single Ni sites anchored carbon nanosheet catalysts for highly efficient carbon dioxide electroreduction, *J. Mater. Sci. Technol.*, 2023, **142**, 1–9.

52 X. Li, X. Wen, J. Lang, J. Wei, J. Miao, X. Zhang, B. Zhou, M. Long, P. J. Alvarez and L. Zhang, CoN_1O_2 single-atom catalyst for efficient peroxymonosulfate activation and selective cobalt(IV)=O generation, *Angew. Chem., Int. Ed.*, 2023, **135**(27), e202303267.

53 M. Kim, K. L. Firestein, J. F. Fernando, X. Xu, H. Lim, D. V. Golberg, J. Na, J. Kim, H. Nara and J. Tang, Strategic design of Fe and N co-doped hierarchically porous carbon as superior ORR catalyst: from the perspective of nanoarchitectonics, *Chem. Sci.*, 2022, **13**(36), 10836–10845.

54 M. Zhang, H. Li, J. Chen, F. X. Ma, L. Zhen, Z. Wen and C. Y. Xu, High-loading Co single atoms and clusters active sites toward enhanced electrocatalysis of oxygen reduction reaction for high-performance Zn–air battery, *Adv. Funct. Mater.*, 2023, **33**(4), 2209726.

55 X. Xie, H. Peng, K. Sun, W. Li, A. Liang, G. Ma, Z. Lei and Y. Xu, A simultaneous modulation strategy to construct high dense and accessible Co–N_4 sites for promoting oxygen reduction reaction in zn–air battery, *Adv. Funct. Mater.*, 2024, 2316037.

56 Y. He, Q. Shi, W. Shan, X. Li, A. J. Kropf, E. C. Wegener, J. Wright, S. Karakalos, D. Su and D. A. Cullen, Dynamically unveiling metal–nitrogen coordination during thermal activation to design high-efficient atomically dispersed CoN_4 active sites, *Angew. Chem., Int. Ed.*, 2021, **133**(17), 9602–9612.

57 Y. Ha, B. Fei, X. Yan, H. Xu, Z. Chen, L. Shi, M. Fu, W. Xu and R. Wu, Atomically dispersed Co-pyridinic N-C for superior oxygen reduction reaction, *Adv. Energy Mater.*, 2020, **10**(46), 2002592.

58 L. Li, P. Dai, X. Gu, Y. Wang, L. Yan and X. Zhao, High oxygen reduction activity on a metal–organic framework derived carbon combined with high degree of graphitization and pyridinic-N dopants, *J. Materi. Chem. A*, 2017, **5**(2), 789–795.

59 J. Gao, N. Ma, Y. Zheng, J. Zhang, J. Gui, C. Guo, H. An, X. Tan, Z. Yin and D. Ma, Cobalt/nitrogen-doped porous carbon nanosheets derived from polymerizable ionic liquids as bifunctional electrocatalyst for oxygen evolution and oxygen reduction reaction, *ChemCatChem*, 2017, **9**(9), 1601–1609.

60 H. Liu, L. Jiang, J. Khan, X. Wang, J. Xiao, H. Zhang, H. Xie, L. Li, S. Wang and L. Han, Decorating single-atomic Mn sites with FeMn clusters to boost oxygen reduction reaction, *Angew. Chem. Int. Ed.*, 2023, **135**(3), e202214988.

61 C. Chen, S. Zhou, J. Xia, L. Li, X. Qian, F. Yin, G. He and H. Chen, g-C3N4 promoted MOF-derived Fe single atoms anchored on N-doped hierarchically porous carbon for high-performance Zn-air batteries, *J. Colloid Interface Sci.*, 2024, **653**, 551–560.

62 B. Yue, K. Yang, H. Xie, Y. Lei, J. Li and Y. Si, Core–shell structured Fe–N–C wrapped by an ultrathin porous carbon shell as a robust electrocatalyst for the oxygen reduction reaction, *New J. Chem.*, 2023, **47**(20), 9735–9745.

63 M. Xiao, H. Zhang, Y. Chen, J. Zhu, L. Gao, Z. Jin, J. Ge, Z. Jiang, S. Chen and C. Liu, Identification of binuclear $Co2N5$ active sites for oxygen reduction reaction with more than one magnitude higher activity than single atom CoN_4 site, *Nano energy*, 2018, **46**, 396–403.

64 H. Zhou, J. Luo and Y. Chen, Nitrogen moieties-dominated Co–N-doped nanoparticle-modified cathodes in heterogeneous-electro-Fenton-like system for catalytic decontamination of EDTA-Ni (II), *Chemosphere*, 2020, **239**, 124743.

65 Y. Li, X. F. Lu, S. Xi, D. Luan, X. Wang and X. W. Lou, Synthesis of N-doped highly graphitic carbon urchin-like hollow structures loaded with single-Ni atoms towards efficient CO2 electroreduction, *Angew. Chem., Int. Ed.*, 2022, **61**(18), e202201491.

66 Z. Deng, S. J. Choi, G. Li, X. Wang and H. Advancing, $2O_2$ electrosynthesis: enhancing electrochemical systems, unveiling emerging applications, and seizing opportunities, *Chem. Soc. Rev.*, 2024, **53**(16), 8137–8181.

14644 | *J. Mater. Chem. A*, 2025, **13**, 14631–14645

This journal is © The Royal Society of Chemistry 2025

67 S. Liu, J. Xue, X. Liu, H. Chen and X. Li, Pitch derived graphene oxides: characterization and effect on pyrolysis and carbonization of coal tar pitch, *J. Anal. Appl. Pyrolysis*, 2020, **145**, 104746.

68 C. Xin, W. Shang, J. Hu, C. Zhu, J. Guo, J. Zhang, H. Dong, W. Liu and Y. Shi, Integration of morphology and electronic structure modulation on atomic iron-nitrogen-carbon catalysts for highly efficient oxygen reduction, *Adv. Funct. Mater.*, 2022, **32**(2), 2108345.

69 G. Zhang, Z. Wu, A. Li, Y. Wang, J. Zhang, M. Abbas, R. Hu, X. Ni, Y. Tong and Y. Hwu, XANES investigation of the local structure of Co nanoclusters embedded in Ag, *Phys. Rev. B: Condens. Matter Mater. Phys.*, 2004, **69**(11), 115405.

70 L. Li, C. Tang, Y. Zheng, B. Xia, X. Zhou, H. Xu and S. Z. Qiao, Tailoring selectivity of electrochemical hydrogen peroxide generation by tunable pyrrolic-nitrogen-carbon, *Adv. Energy Mater.*, 2020, **10**(21), 2000789.

71 G. Kresse and J. Hafner, Ab initio molecular dynamics for liquid metals, *Phys. Rev. B: Condens. Matter Mater. Phys.*, 1993, **47**(1), 558–561.

72 G. Kresse and J. Furthmuller, Efficient iterative schemes for *ab initio* total-energy calculations using a plane-wave basis set, *Phys. Rev. B: Condens. Matter Mater. Phys.*, 1996, **54**(16), 11169–11186.

73 G. Kresse and J. Furthmuller, Efficiency of *ab initio* total energy calculations for metals and semiconductors using a plane-wave basis set, *Comput. Mater. Sci.*, 1996, **6**(1), 15–50.

74 J. P. Perdew, K. Burke and M. Ernzerhof, Generalized gradient approximation made simple, *Phys. Rev. Lett.*, 1996, **77**(18), 3865–3868.

75 P. E. Blochl, Projector augmented-wave method, *Phys. Rev. B: Condens. Matter Mater. Phys.*, 1994, **50**(24), 17953–17979.

76 G. Kresse and D. Joubert, From ultrasoft pseudopotentials to the projector augmented-wave method, *Phys. Rev. B: Condens. Matter Mater. Phys.*, 1999, **59**(3), 1758–1775.

77 S. Grimme, J. Antony, S. Ehrlich and H. Krieg, A consistent and accurate *ab initio* parametrization of density functional dispersion correction (DFT-D) for the 94 elements H-Pu, *J. Chem. Phys.*, 2010, **132**(15), 154104.

78 H. Lipson and A. R. Stokes, The structure of graphite, *Proc. R. Soc. London, Ser. Math. Phys. Sci.*, 1942, **181**, 101–105.

79 X. Zhang, Y. Li, H. Zhang and G. Li, Fast capture and stabilization of Li-ions *via* physicochemical dual effects for an ultra-stable self-supporting Li metal anode, *Carbon Energy*, 2023, **5**(9), e348.

80 H. J. Monkhorst and J. D. Pack, Special points for Brillouin-zone integrations, *Phys. Rev. B: Condens. Matter Mater. Phys.*, 1976, **13**(12), 5188–5192.

81 B. Huang, X. Zhao and Y. Pei, First principles calculation study of single transition metal atom grafted Au25 as efficient electrocatalysts for OER and ORR, *Mol. Catal.*, 2023, **540**, 113030.

82 C. Ling, L. Shi, Y. Ouyang, X. C. Zeng and J. Wang, Nanosheet supported single-metal atom bifunctional catalyst for overall water splitting, *Nano Lett.*, 2017, **17**(8), 5133–5139.

83 X. Zhang, Z. Yang, Z. Lu and W. Wang, Bifunctional CoN_x embedded graphene electrocatalysts for OER and ORR: a theoretical evaluation, *Carbon*, 2018, **130**, 112–119.

84 V. Wang, N. Xu, J.-C. Liu, G. Tang and W.-T. Geng, VASPKIT: a user-friendly interface facilitating high-throughput computing and analysis using VASP code, *Comput. Phys. Commun.*, 2021, **267**, 108033.

This journal is © The Royal Society of Chemistry 2025

J. Mater. Chem. A, 2025, **13**, 14631–14645 | **14645**